Available online at www.sciencedirect.com

jmr&t Journal of Materials Research and Technology

journal homepage: www.elsevier.com/locate/jmrt

Quantitative analysis of pore characteristics of nanocellulose reinforced cementitious tailings fills using 3D reconstruction of CT images

Aiai Wang [a,b], *Shuai Cao* [a,b,*], *Erol Yilmaz* [c,**]

[a] *State Key Laboratory of High-Efficient Mining and Safety of Metal Mines of Ministry of Education, University of Science and Technology Beijing, Beijing 100083, China*

[b] *School of Civil and Resource Engineering, University of Science and Technology Beijing, Beijing 100083, China*

[c] *Department of Civil Engineering, Geotechnical Division, Recep Tayyip Erdogan University, Fener, Rize TR53100, Turkey*

ARTICLE INFO

Article history:
Received 27 February 2023
Accepted 1 August 2023
Available online 4 August 2023

Keywords:
Cementitious fill
Nanocellulose
Double pore network
Microstructure
Pore fracture features

ABSTRACT

This study aims at analyzing the influence of contents and types of various nanocelluloses (e.g., CNF, CNC, and MFC) and intermediate microstructure on strength/fracture features of cementitious tailings backfill (CTB). This is important in understanding the environmental implications of tailings and crushed rock accumulation. Researchers explored the strength behavior of nanocellulose-reinforced CTB (NRCTB) while analyzing quantitatively their spatial structure/fractures through SEM and CT (computed tomography) methods. Results highlight that optimizing the content of nanocelluloses can boost the pore structure of NRCTB. CTB reinforced with CNF and CNC exhibit specific pore structures, while MFC-CTBs shows a different pattern. The addition of nanocellulose helps in suppressing cracking. The overall porosity of the different CTB samples varied. The study also proposes a dual nanocellulose-pore network model to explain the microscopic enhancement mechanism. The findings subsidize the understanding of NRCTB's microscopic enhancement mechanisms and can have implications for mitigating environmental damage caused by tailings-crushed rock accumulation.

1. Introduction

From the basis of carbon peaking and carbon neutral era, cementitious tailings backfill (CTB: a new composites consisting usually of tailings, cement and water [1,2]) promotes green, low carbon, recycling and sustainable development of traditional mines [3] and is extensively used in mines at home and abroad [4]. Therefore, technologies that provide relatively high energy and low carbon emissions will become first priorities in the value chain in civilization [5,6]. In fact, industries such as iron and steel, non-ferrous, chemical and cement

* Corresponding author. State Key Laboratory of High-Efficient Mining and Safety of Metal Mines of Ministry of Education, University of Science and Technology Beijing, Beijing 100083, China.
** Corresponding author.
E-mail addresses: WangAiAi_WAA@163.com (A. Wang), sandy_cao@ustb.edu.cn (S. Cao), erol.yilmaz@erdogan.edu.tr (E. Yilmaz).
https://doi.org/10.1016/j.jmrt.2023.08.004

consume high energy and face these defies [7]. Zero-carbon steel/cement/buildings [8] have emerged, and bio-based materials have recently appealed lots of research concerns since they have great potential to create many high-value goods having less ecological effects [9]. Several scholars explored the influence mechanism of external additives such as flocculant [10], fly ash [11], desulfurized gypsum [12] and water reducer [13] on CTB's strength. Researchers also recognized that the fill's strength is principally linked to its curing age [14], slurry concentration [15], additive type [16], and efficient lab tool [17]. Nanocellulose (NCM) has several benefits such as high strength/elastic modulus [18], large specific surface [19], and durable hydrophilicity [20]. It can inhibit crack growth at the nanometer scale, and has a physical filling effect [21]. It improves the composite's microstructure and the strength behavior of cemented materials [22]. Being a crystalline part of cellulose molecules, NCM has some properties such as biodegradability/sustainable regeneration [23] and high purity/crystallinity/transparency [24]. Varisha et al. [25] selected four different NCM aqueous suspensions to evaluate the impact on the final performance of mortar, and obtained that CNC was more effective in improving the compressive strength (up to 21%). Haque et al. [26] explored the application of diverse NCMs such as CNF, BNC and CNC within cement-based composites. The effects of some NCM materials (e.g., CNC, CNF, and MFC) on strength development of filling were experimentally explored [27]. Stephens et al. [28] also shows that the addition of CNF bending and bending strength increases. Fan et al. [29] showed that the addition of 0.3% CNC as a reinforcing agent to the mixture resulted in a 22% increase in compressive strength. MFC interacts more strongly with OPC hydration products, which may result in delayed cure, increased hydration and improved mechanical properties. Siqueira et al. [30] also indicated that NCMs could reduce cracking due to thermal shrinkage and stress induced by structural constraints.

Relevant discussions on this important aspect were made by some scholars. Cui et al. [31] proposed a series of image analysis methods such as industrial-, micro-, and nano-CT and fluids. The shale pores were characterized by injection method. Chalmers et al. [32] believed that a multidisciplinary method was needed to evaluate the pore distribution of fine-grained sedimentary shale reservoirs, and a single method could not evaluate shale reservoirs in detail. Organic petrology, FE-SEM and BSE microscope were used to jointly confirm its microscopic composition [33]. Although the fusion of multiple methods has solved the multi-scale problem of shale pore characterization to a certain extent, since the pore testing principles and theoretical foundations of various methods are diverse [34], the key to the fusion of multiple methods is to ensure that similarities in pore test principles, such as fusion of fluid injection methods, fusion of diverse scale image analysis, and fusion of non-fluid injection methods [35]. Pore characterization covers image analysis, fluid injection (e.g., mercury intrusion, gas adsorption and other fluid injection) and non-fluid injection. These methods can reveal the structure and distribution characteristics of pores [36–38]. Ghamgosar et al. [39] adopted 3D CT scan technique to analyze the images of rock under cyclic loads, determined crack propagation/evolution mode in rock failure, and found that initiation/aggregation of micro cracks during the rock failure are the main characteristics of crack propagation in rock. Kumari et al. [40] conducted CT experiments on propagation of cracks in granite under compression conditions, and studied the propagation path of cracks from macro/micro scales. The study showed that the propagation path of cracks was primarily governed by the rock's stress state/heterogeneity while cracks tended to propagate and evolve along mineral grain limits and big-grained quartz and biotite. Wang et al. [41] extracted cracks of diverse scales from CT images at diverse deformation stages by combining 3D reconstruction system with image threshold segmentation. By recording the processes of crack closure, generation, expansion and penetration, they found that the existence of banded pyrite affects the initiation and evolution of cracks [42]. CTB is a heterogeneous porous material with a complicated micro-structure having gel/capillary pores [43–45]. The backfill pores are related to the mechanical properties and transmission performance [46], and characterized by the X-ray CT scan method which is adopted to obtain not only conventional pore parameters but also open pores, closed pores, effective connected pores and ineffective connected pores [47–49]. The transmission performance of concrete can be studied through the connectivity of pores [50].

The pore defects within CTB make a great contribution to the development of cracks [51]. The macro distortion of specimens under external loadings is recognized by modifying the interior microstructure factors [52–55]. As a non-invasive/destructive image technique, CT scan has been used for a long time to detect the internal structure of materials [56]. Xue et al. [57] detected the crack growth of fiber reinforced backfills by UCS tests, revealing the destruction process of interior structure. Bharath et al. [58] employed CT system to detect grouting effect of cement asphalt slurry, and analyzed the proportion of crack volume and connectivity in the grouting body. Tian et al. [59] studied the meso-damage evolution process of specimen through CT scan image of concrete specimen, and quantitatively characterized the specimen's failure process [60]. The images captured in combination with CT scan technique are transformed to mathematical models or 3D pictures by many imaging codes so as to analyze the cemented product's internal structure more quantitatively and intuitively [61–65]. In addition, in combination with stereology and fractal theory, Jianhua et al. [66] explored the cross-scale correlation characteristics between SEM image quantitative analysis and mesoscopic parameters of CTB, and revealed the mechanism of pore structure on its strength development. Hu et al. [67] obtained pore characteristics of diverse aerated fill concrete by PC image science method, and then analyzed the effect of pore properties on concrete's strength/frost resistance [68]. As capturing the inner structure evolution of CTB subjected to external load is a challenging task, numerical simulation is of great significance to reveal its damage and fracture mechanism. Gang et al. [69] conducted conjugate heat transfer simulation/thermal deformation simulation on coal micro-pore fracture structure (3D model reconstructed by CT) using the ANSYS software to study the temperature effect on coal seepage/pore fracture structure deformation [70]. Li et al. [71] scrutinized link between strength and crack width/volume of specimens by industrial CT and SEM, and

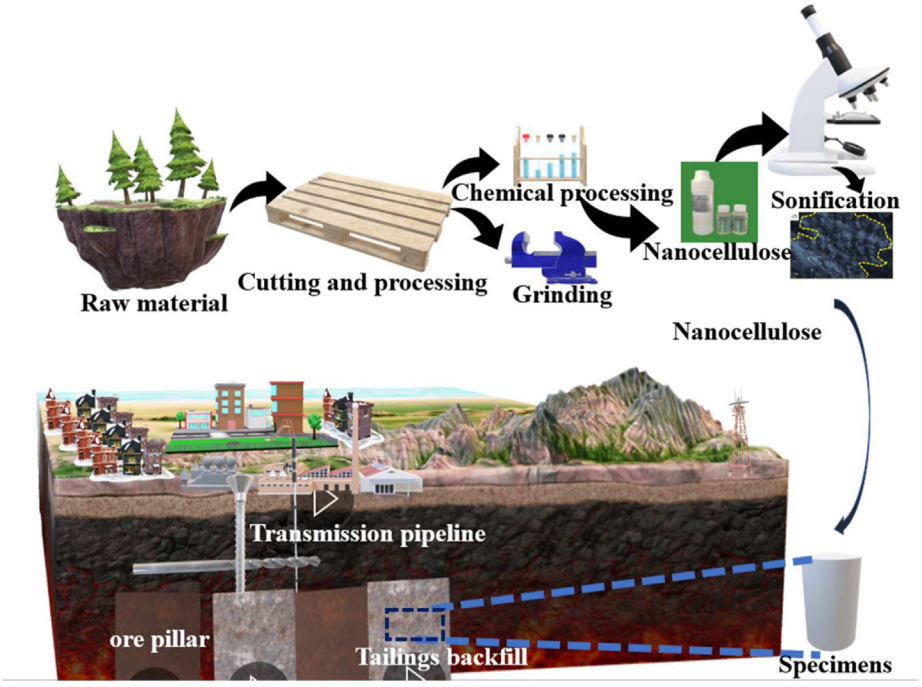

Fig. 1 – Schematic diagram of NCM reinforced backfills adopted in underground mines.

demonstrated that incorporating fibers expressively increased CTB's strength features and meritoriously improved the toughness of CTBs as a task of different backfill recipes.

Above-given works reviewed the existing status of investigation on the implementation of NCM in CTB materials and the strength properties of CTB by CT scan techniques and the means of detection. To enhance the academic rigor of this study on evaluating the pore structure of NCM reinforced fills (Fig. 1) under uniaxial compression, we have made the following advancements and incorporated innovative approaches: 1) Combination of damage mechanics and image processing techniques: This study integrates the principles of damage mechanics with advanced image processing methods to assess the pore structure of NCM reinforced backfills. By utilizing CT scan techniques and image processing algorithms, the three-dimensional (3D) structural characteristics of NCM reinforced CTBs can be truly analyzed and quantified. 2) Quantitative functional relationships: This study creates quantitative functional links among important parameters such as porosity, CT number, fractal dimension, and compressive strength. It aids a systematic analysis of how these parameters affect the strength features of NCM reinforced fills, providing valuable insights into the underlying mechanisms. 3) Deeper understanding of structure-strength correlation: By inspecting the 3D structure of NCM reinforced fills, this study aims at untying the inner link mechanism between the structure and strength properties. This deeper understanding enhances the knowledge base of backfill mechanics and contributes to the optimization of strength and stability control in deep mining fill bodies. In summary, the combination of damage mechanics and image processing techniques, along with the establishment of quantitative functional links, offers an innovative approach to studying NCM reinforced fills. The insights gained from the present investigation have influential theoretical effects and practical applications for fill mechanics field in deep mining operations.

2. Materials and methods

2.1. *Materials*

New green low carbon filling material has been recently proposed in China. In other words, NCMs are mixed into cementitious tailings to form a new filling type called NRCTB (nanocellulose reinforced cemented tailing backfill). Thus, the tailings graded from a mine were used. CNF, CNC, and MFC were selected as a blending NCM. Table 1 shows the content of NCMs. Type 42.5 ordinary Portland cement was designated as a binding agent to create various NRCTB specimens. Type 42.5 OPC's/Tailings' grain size distribution was determined by laser

Table 1 – Nanocellulose content of CTBs (wt.%).

Types	Diameter	Length	State	Concentration (%)
CNF–C/P2.5	4–10 nm	1–3 μm	99.6% powder	0, 0.009, 0.014, 0.019, 0.024
C–CNC	4–10 nm	100–500 nm	99.6% powder	
MFC	0.1–1 μm	>20 μm	Aqueous dispersion	
C–CNC	4–10 nm	100–500 nm	99.6% powder	0, 0.01, 0.02, 0.03, 0.04

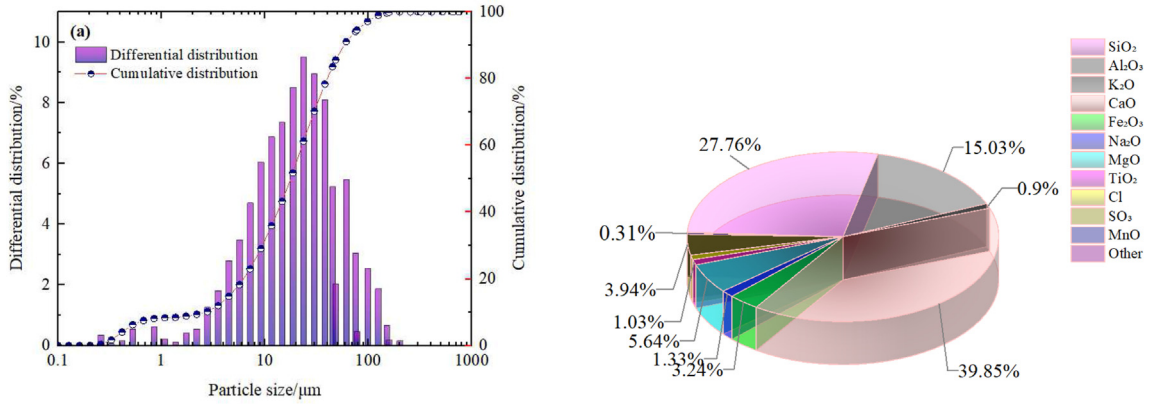

Fig. 2 – The cement's grain size distribution charts: (a) distribution; and (b) composition.

particle sizer, as evidently indicated in Figs. 2 and 3. Six types of tailings fill samples were used in the uniaxial compression tests: CNC-0.009%, CNC-0.014%, CNC-0.019%, CNC-0.009%, MFC-0.009%, and NONE. In this study, a subset of specimens underwent CT scanning after the uniaxial compression tests.

2.2. *Samples preparation*

The amount of test materials required was calculated first and then added to the backfill mixture. NCM needs to be dispersed before being put into the mixing tank, all kinds of materials are stirred evenly in the mixing tank, and then put in φ50 × 100 mm cylindrical mold. After pouring, the molds are left for 48 h first and then detached to get CTB specimens only. CTBs are placed in a cure holder for 7 d curing. Upon curing, CTB's upper/lower surfaces are smoothed, the factors such as heights/weights are measured, and then specimens are subjected to the UCS tests.

3. Experimental procedures

3.1. *UCS experiment*

CTB's strength gaining was determined by a WDW-100 automatic complete test machine which has a 1 mm/min displacement ratio. Several information like UCS and deformation are automatically acquired through a laptop. At least 3 NRCTB specimens for a given backfill recipe was tested through UCS test. Compression for all samples was monitored in real-time while recording stress-strain data concurrently. The compression was considered complete and test was stopped when the deformation plot reached its highest stress and started to drop. The maximum stress stopping criterion is based on previous observations and knowledge of the tailings fill behavior.

3.2. *SEM micro-graphs*

Zeiss Evo 18 SEM-EDS spectroscopy was employed to examine the NRCTB's fracture surface, and to explore the inner structure of 7-day cured NRCTB specimens. EDS offers elemental/chemical analysis of the broken NRCTB specimens. The principal testing factors are as follows: 3 nm resolution; 20 kV accelerating voltage; 5-1,000,000 amplification factor, and 20 keV main energy.

3.3. *CT 3D reconstruction*

An efficient image system, X-ray CT (it compiles 2D image projected by a body, Fig. 4) is employed to recreate CTB's

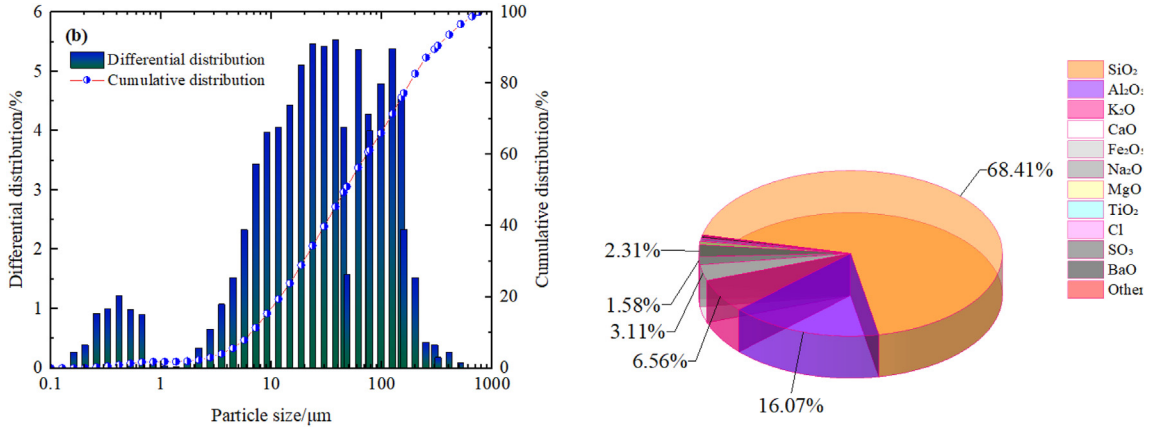

Fig. 3 – The tailings' grain size distribution charts: (a) distribution; and (b) composition.

interior structure attributing into 3D images [72]. It covers X-ray source/head, flat panel sensor, scan device, rebuilding and scan control. CT scan's basic factors are: 3lp/mm spatial resolution, 6 MeV X-ray energy, and 196 mm max. depth of steel. CT scan is respectively used for identify according to the variances of grains, pore and water density of CTB, a 3D digital core body is established, and the existence and attachment forms of pore structures, cracks and NCM are gained [73–75]. 3D reconstruction system, which is preferred in the lab to analyze the microstructures of the fills utilized in mines, is very vital for researchers because it gets it easy to make critical decisions about the backfilling in terms of cost and performance. A visualization software was employed for 3D reconstruction of piece pictures. To stop edging impacts, 3D reconstructed model's limits were erased, Avizo software is then used to binarize a derived 3D grayscale image, to divide pore-grain matrix, and to get a segmented image that can be used for pore modeling (Fig. 5).

3D structural features like pore size, number/fractal connectivity of NCM backfilled bodies were obtained by region selection and noise reduction of grayscale images, and the different components were divided and counted. Firstly, the three-dimensional structure, i.e., the fractal dimension of nanocellulose backfilled body and pore fissures, was solved by the fractal theory and counting box dimension technique, and then the change pattern of damage presented by different types of nanocellulose backfilled body fine structure was analyzed by combining with CT.

4. Results and discussion

4.1. *Spatial distribution features of multi-scale internal modules*

After data acquisition and reconstruction, the substances with different densities in the actual samples were divided according to the gray value domain. The diverse gray modules of CT images were calibrated and further divided according to the principle that the CT images' gray value reflects the link between the density of substances, combined with the results of the identification of minerals on the surface of CTB particles by electron microscopy, in which the gray value > 1000 is considered as high-density substances, usually nanocellulose, marked as red. The grayscale values in the range of 1–470 are considered as pore structures and are marked as gray. The gray value range of 650–1000 is medium-density material, mostly minerals and chemical products within CTB; the dark gray part (i.e., gray value range of 470–650) is low-density material, mostly cracks in CTB, and is marked as blue. The three components, pores, micro cracks and nanocellulose, were extracted to attain an intuitive three-dimensional distribution map. The further pixel counts of the gray value domains were performed separately to obtain the pores' distribution, micro cracks and nanocellulose in the backfill specimens.

4.1.1. *2D slice characterization techniques*

Fig. 6 indicates the morphological characteristics of NCM within CTBs which are diverse in terms of the NCM types used in the mix. From the perspective of nanocellulose morphology, CNF and CNC are uniformly distributed, showing a clear honeycomb structure with full-scale distribution characteristics. Nanocellulose is filled in 'small pores' with a span of below 300 nm, and in 'large pores' with a span of more than 300 nm. Nanocellulose is presented as a thin film on pore/fill's surface. MFC is mainly devoted to the surface of grains, inter- and large-pores, and the physical form is isolated. Nanocellulose contributes to the reduction of surface fracture expansion and the enhancement of microstructure density.

Fig. 7 also displays that pores' morphological features within different nanocellulose CTB specimens are different. In terms of pore morphology, the pores of CNF and CNC

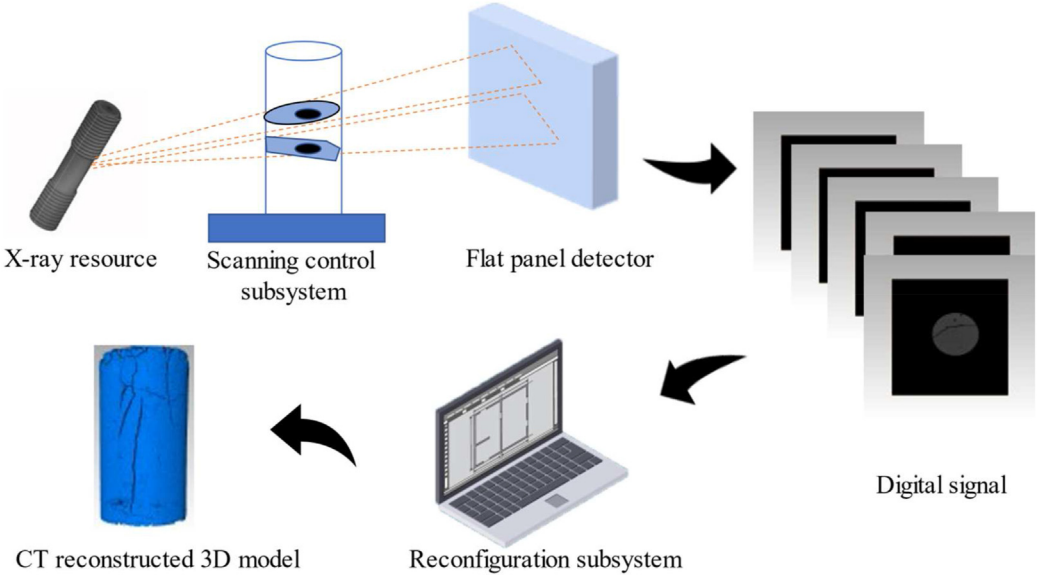

Fig. 4 – Computed tomography (CT) test system technique schematic diagram.

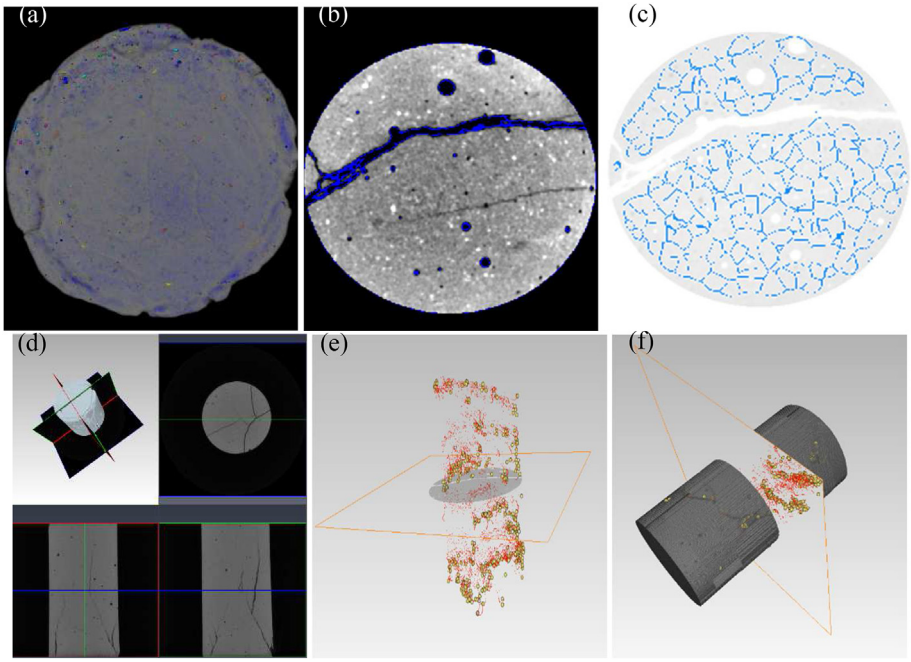

Fig. 5 – Nanocellulose fill's 3D reconstruction model: (a) 3-phase scanned image; (b) pore scan image; (c) NCM interpolation chart; (d) 3D multiscale depiction; (e) NCM extraction model; and (f) 3D reconfiguration model.

reinforced CTBs have a small number of large pores, which are cylindrical in shape, and these large pores are isolated; the small pores as a whole show a uniform distribution of dispersed or mineral-backfilled pores, and none of pores and fissures are connected. The pores of MFC-CTBs are dominated by slit-type pores, which is in keeping with the SEM observations. Pore characteristics show a fickle pore size and random distribution of pores, with a high number of pores overall.

4.1.2. *Two-dimensional fracture multi-scale characterization techniques*

Fig. 8(a), (b) and (c) show CT scan features of CNF, CNC, MFC and no nanocellulose added CTB specimens, respectively. Blue represents the specimen and black represents the internal fissures, which appear as long fissures. Comparing the CT scans of the internal structure of specimens, it can be seen that the CTB specimens without nanocellulose show dendritic fissures, with wider and more fissures, three main fissures penetrating specimens and expanding to create new fissures and extending multiple micro cracks, with the fissures penetrating to form a large fissure network. NCM was added to specimens, which had an inhibiting effect on cracks. It can be found that the fracture width of CTB specimens with NCM is significantly smaller than the fracture width of control CTB specimens. In the observations of CNC-CTBs specimens, the fracture development inside the specimen extends from the end point and bifurcates in a Y-shape, the blue line is the fracture profile line, the fractures are narrower and less numerous, distributed throughout the area without interpenetration. It is because the fractures inside specimen are sealed by nanocellulose backfill, the main fracture length is shorter, dividing the remaining fracture part into several small fracture segments (as shown in the horizontal section of Fig. 8(a), the micro fractures were discrete and the overall

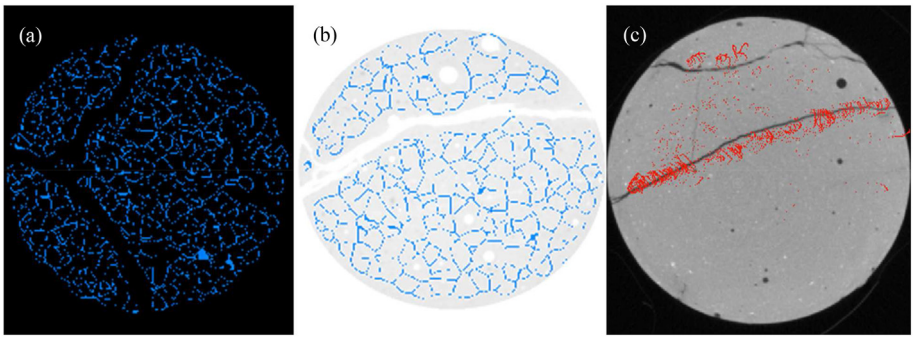

Fig. 6 – Nanocellulose distribution of CTBs: a) NCF, b) CNC, and c) MFC.

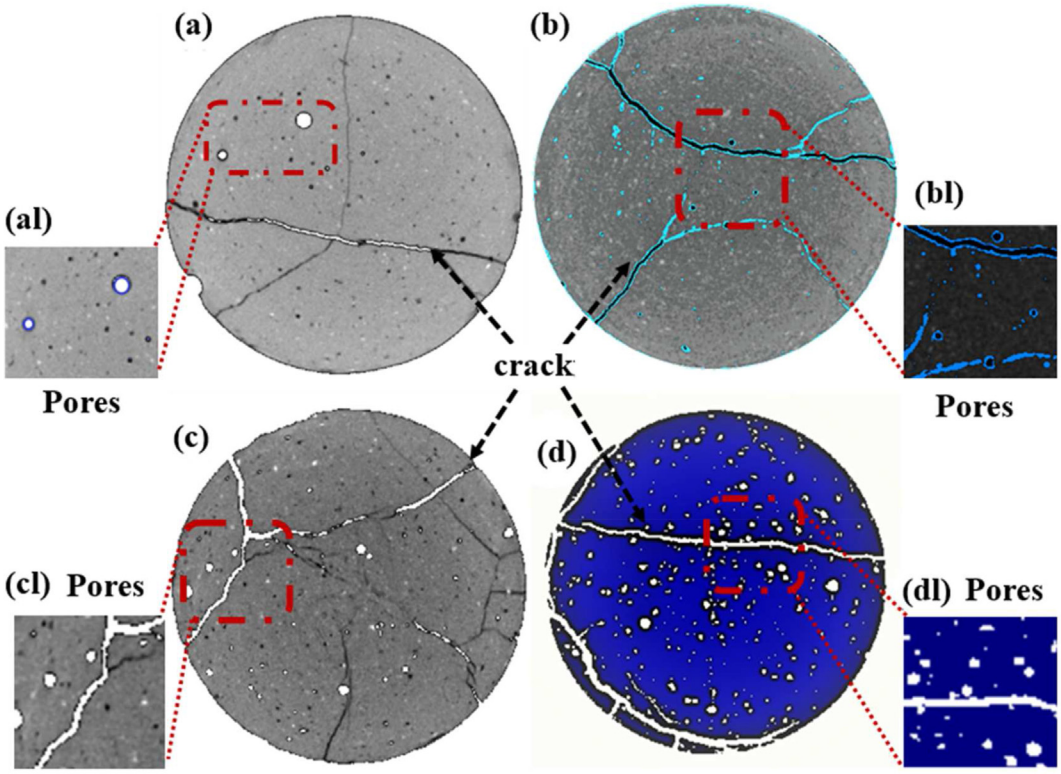

Fig. 7 – Comparison of structural features and local fine characterization of CT pores in CTBs: (a) CNF-CTBs pore 2D section (a1) a-plot local enlargement; (b) CNC-CTBs pore 2D section (b1) b-plot local enlargement; (c) MFC-CTBs pore 2D section (c1) c-plot local enlargement; (d) CTBs pore 2D section (d1) Local enlargement of d-plot.

crack connectivity was poor; whereas the last horizontal section of control backfill fractures formed a crack network with the adjacent vertical fractures.

4.1.3. *Characterization techniques for pores'/NCM's 3D spatial distribution*

In this study, the Otsu technique is employed to control the inauguration for segmentation, and then watershed algorithm is used for the separation of adjacent pores. According to 3D reconstruction model, spatial distribution pattern of pores, nanocellulose and mineral matrix (spheres are isolated pores, red is NCM and gray is the CTB matrix) can be obtained. NRCTB interacts with pores and NCM is uniformly distributed in the pore fissures; NCM is clustered into groups with different morphology. The spatial distribution and contact link between filling matrix and pores are seen in Fig. 9 (g), (h) and (i), which clearly displays the dissemination of the pore fractures within CTB specimens. Pores are scattered in all

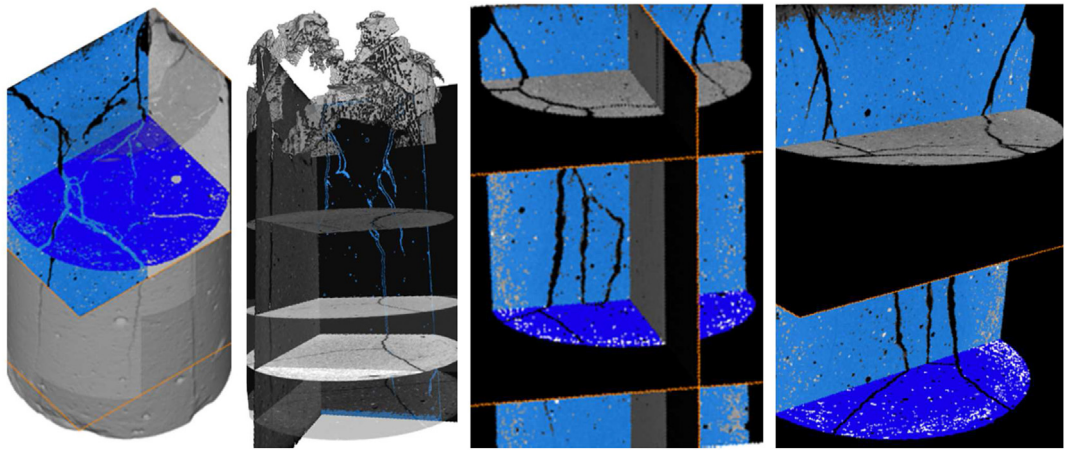

Fig. 8 – Comparison of structural features and local fine characterization of CT fractures in tailing sand-filled bodies: 2D sections of CNF-CTBs (a), CNC-CTBs (b), and MFC-CTBs (c) fractures.

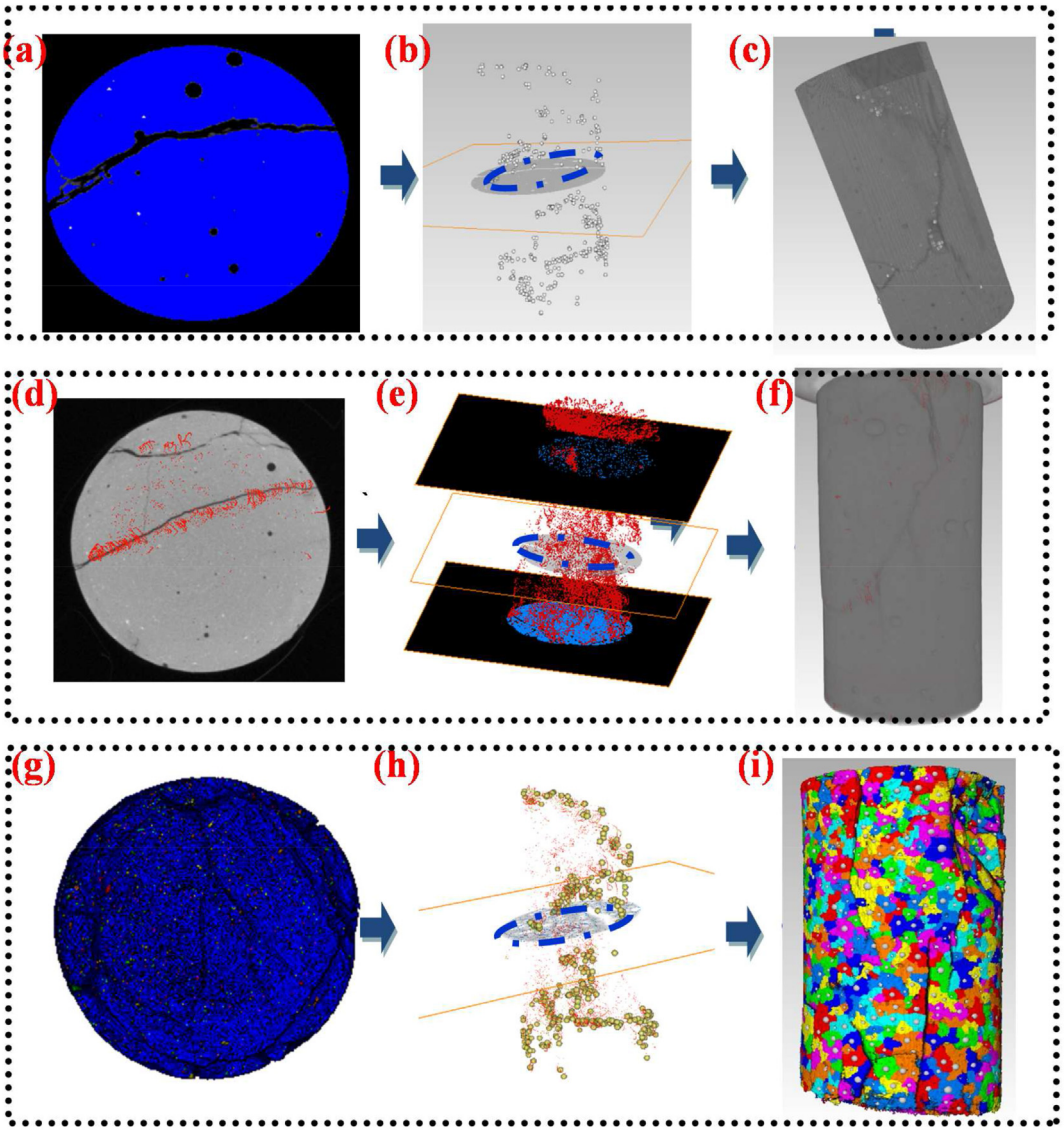

Fig. 9 – Image processing procedures: (a) pore scan section; (b) pore 3D spatial distribution; (c) pore specimen stereo 3D modeling; (d) nanocellulose scan section; (e) nanocellulose 3D spatial distribution; (f) nanocellulose specimen stereo 3D modeling; (g) three-phase scan section; (h) nanocellulose-pore 3D spatial distribution; and (i) specimen stereo 3D modeling.

areas of the model, with pore sizes varying and the morphology of large and fine pore sizes varying, with the large pore sizes having good penetration, while fine pore sizes are scattered in all spaces.

From Fig. 10, one can see the distribution of diverse NCM types/contents within specimens, from the morphology of NCM, CNF and CNC are evenly distributed, showing an obvious complex honeycomb structure with full-scale distribution characteristics, the nanocellulose in the 'small pores' with small relative radius is filled, and NCM in the 'large pores' with large relative radius is in a form of thin film on pore's surface or fill's surface. Nanocellulose in the "small pores" with small relative radius is filled, and NCM in the 'large pores' with large relative radius is deposited on the pore surface or the surface of the filler in a thin film.

Fig. 10 (a) shows that the NCM content of the tailing sand filler is low, and the NCM content is not enough to form a honeycomb mesh structure, which cannot effectively fuse the pores to enhance the strength of the specimen. The CNC-CTBs in Fig. 10(b) shows an obvious complex honeycomb structure with full-scale distribution characteristics, and the nanocellulose fills the small pores so that the CTBs is combined as a whole; the CNC-CTBs in Fig. 10(c) is dominated by the floc mesh cluster, and the flocs occupy most of the space, and the nanocellulose flocs become the porous media skeleton of CTBs, so that specimens can be strengthened by nanocellulose With increasing volume/surface area/pore water of CNC-CTBs, and it is more tough to take away water, which reduces specimen's strength.

3D reconstructed model of MFC-CTBs was interspersed with nanocellulose, which was distributed in strips in the matrix of CTBs. Combining the three-dimensional model with the cross-sectional images, it can be found that MFC-CTBs' pores are of various scales and have cross-scale

characteristics as a whole, and MFC presents a shelf-like structure in the CTB matrix also forms large pore size pores, and the formation of MFC-CTBs' pores is influenced by the distribution of MFC, so pore structure is so linked to the content and decomposition of NCM.

4.2. *Quantitative characterization of multi-scale pore and fissure structures*

4.2.1. *Pore characteristics*

The difference in pore volumes of different NRCTB is large, and the number of pores of CNC-CTBs is about twice that of MFC-CTBs, while the difference in pore volumes of different specimens is small. Fig. 11 shows the pore volume distribution of the four specimens, and it can be seen that the pore volumes of the four specimens are mostly between 0.01 and 0.02 mm^3. Statistical analysis shows that the pore volume of NRCTB has a large variability, reflecting the inhomogeneity of pore shape and volume of NRCTB composition. After qualitative analysis and quantitative calculation of the CT scan pore volumes of different NRCTB, it was found that 68.03% of CNC-CTBs were between 0.01 and 0.02 mm^3, and their average pore volumes were 0.015 mm^3; 60.57% of CNF-CTBs volumes were between 0.01 and 0.02 mm^3, and their mean volumes were 0.017 mm^3, with less variability between pore structures. 24.49% of the pore volumes of MFC-CTBs ranged from 0.015 to 0.02 mm^3, 15.34% ranged from 0.025 to 0.03 mm^3 and 10.34% ranged from 0.035 to 0.04 mm^3, with greater variability in pore number and greater variability between pore volumes. In blank control group, 64.96% were between 0.01 and 0.02 mm^3, and the variability of pore structure was smaller due to the similar causes of pore formation. The reason for this is that CNC is 3.07% more than the blank control group in the pore volume between 0.01 and 0.02 mm^3, because CNC is uniformly distributed with full size distribution features, and nanocellulose is filled in the large pores with pore volume greater than 0.02 mm^3. The quantification illustrates that adding MFC augmented the backfill matrix pores. The existence of MFC augmented the amount of the pores connected within CTB and enhanced MFC-CTBs' porosity.

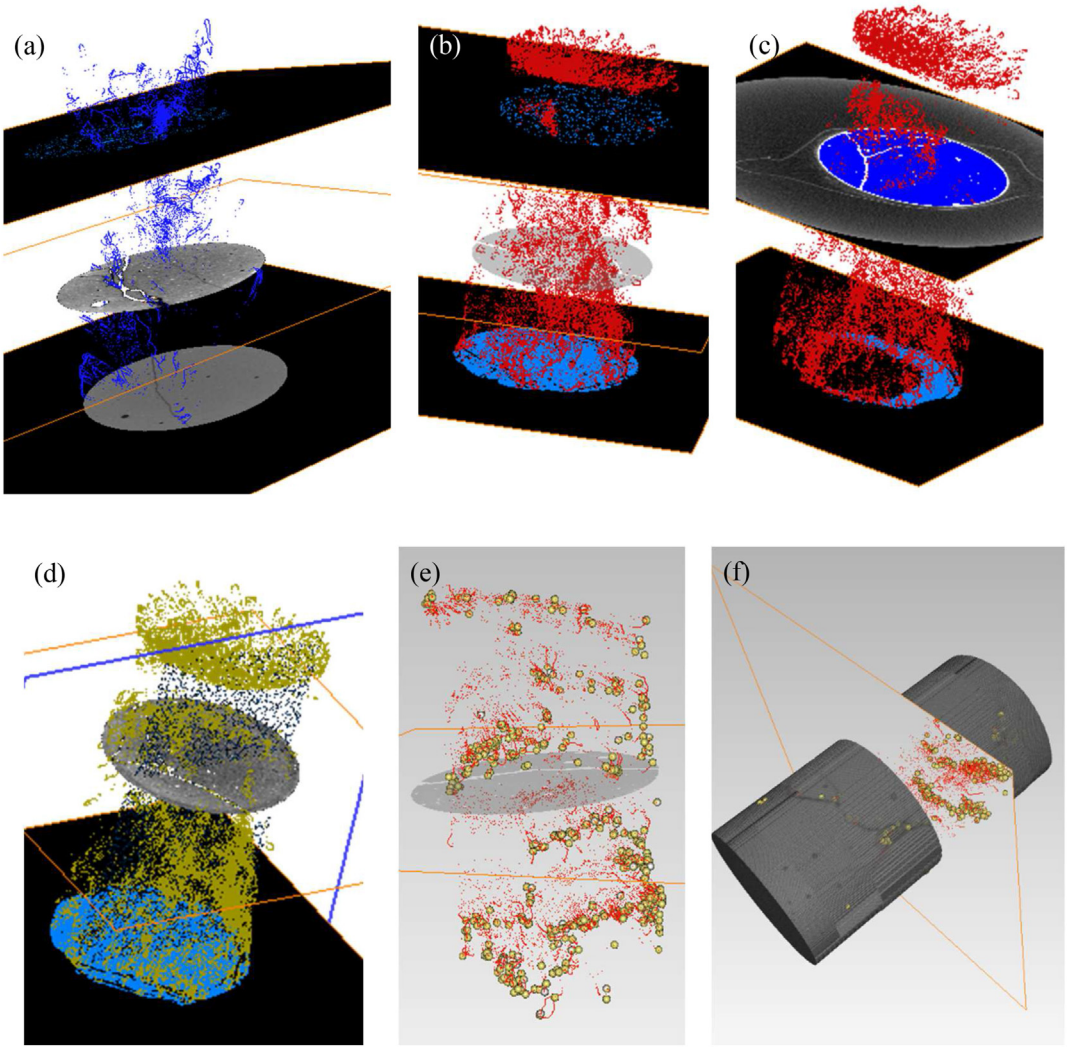

Fig. 10 – 3D spatial distribution of different types and concentrations of NCM: (a) CNC-0.009%; (b) CNC-0.014%; (c) CNC-0.019%; (d) CNC-0.009%; (e) MFC-0.009%; and (f) NONE.

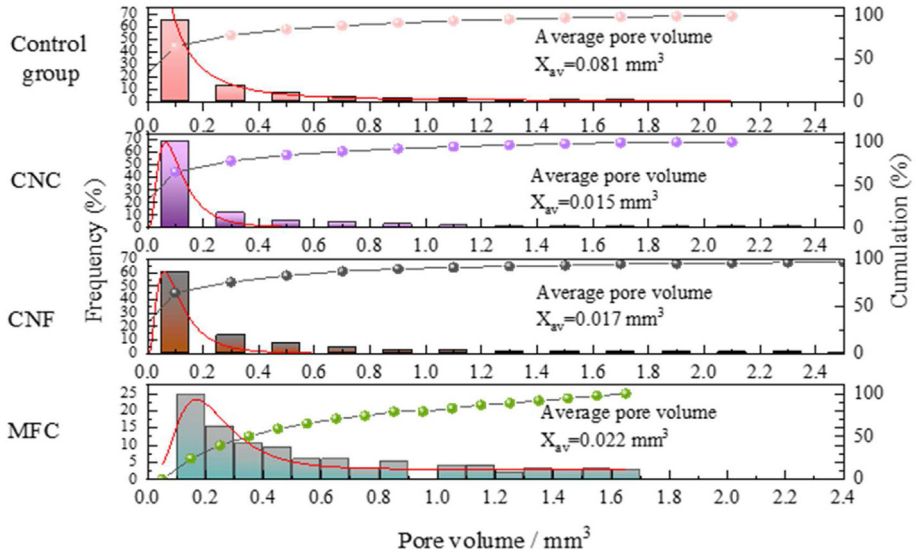

Fig. 11 – Particle size distribution of different NRCTB' pore volumes.

4.2.2. *Porosity*

Porosity is the rate of bulk elements to entire elements of pores. Porosity is one of key considerations to characterize the inner configuration of coal particle accumulation, and 3D reconstructed model's porosity is computed according to Eq. (1):

$$\varepsilon = \frac{V_{solid}}{V_{all}} \tag{1}$$

Among them, ε is the porosity; V_{solid} is the number of pore voxels in reconstructed model; V_{all} is the number of all voxels in reconstructed model. The trends of porosity of different NCM-CTBs are shown in Fig. 12.

The porosity of CNC is lower at 5.64% with less variation, and the porosity is concentrated at less than 10%, indicating that the internal microstructure of CNC-CTBs is more stable; for the scanned CNF-CTBs, the porosity is 11.8% porosity is concentrated at 10%–20%, and the internal microstructure of its CNF-CTBs is also more stable; the porosity of MFC-CTBs was higher at 19.56%, the minimum porosity was 14%, and the maximum porosity was 81%, which was 8 times higher than that of CNC-CTBs, and the porosity was more variable

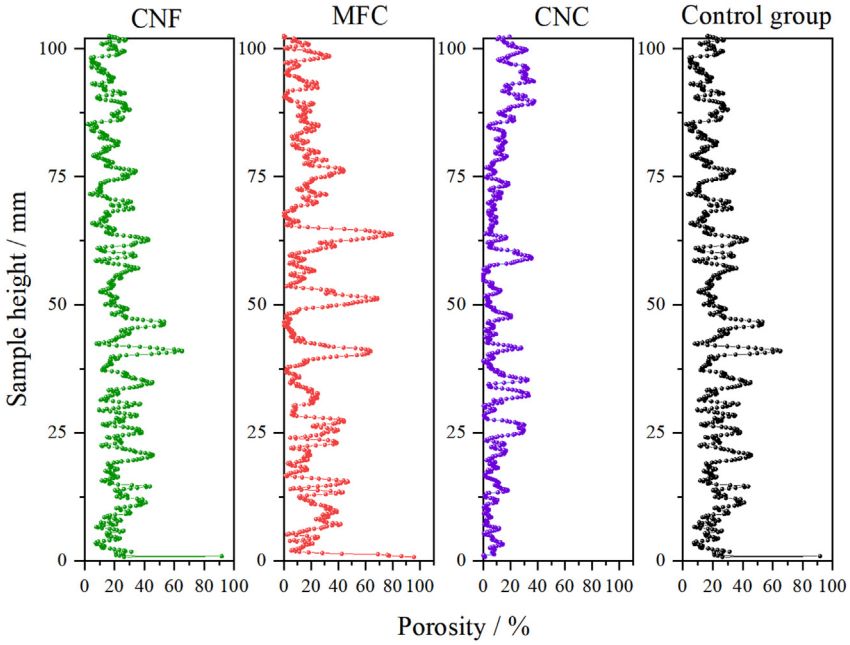

Fig. 12 – Porosity along vertical direction.

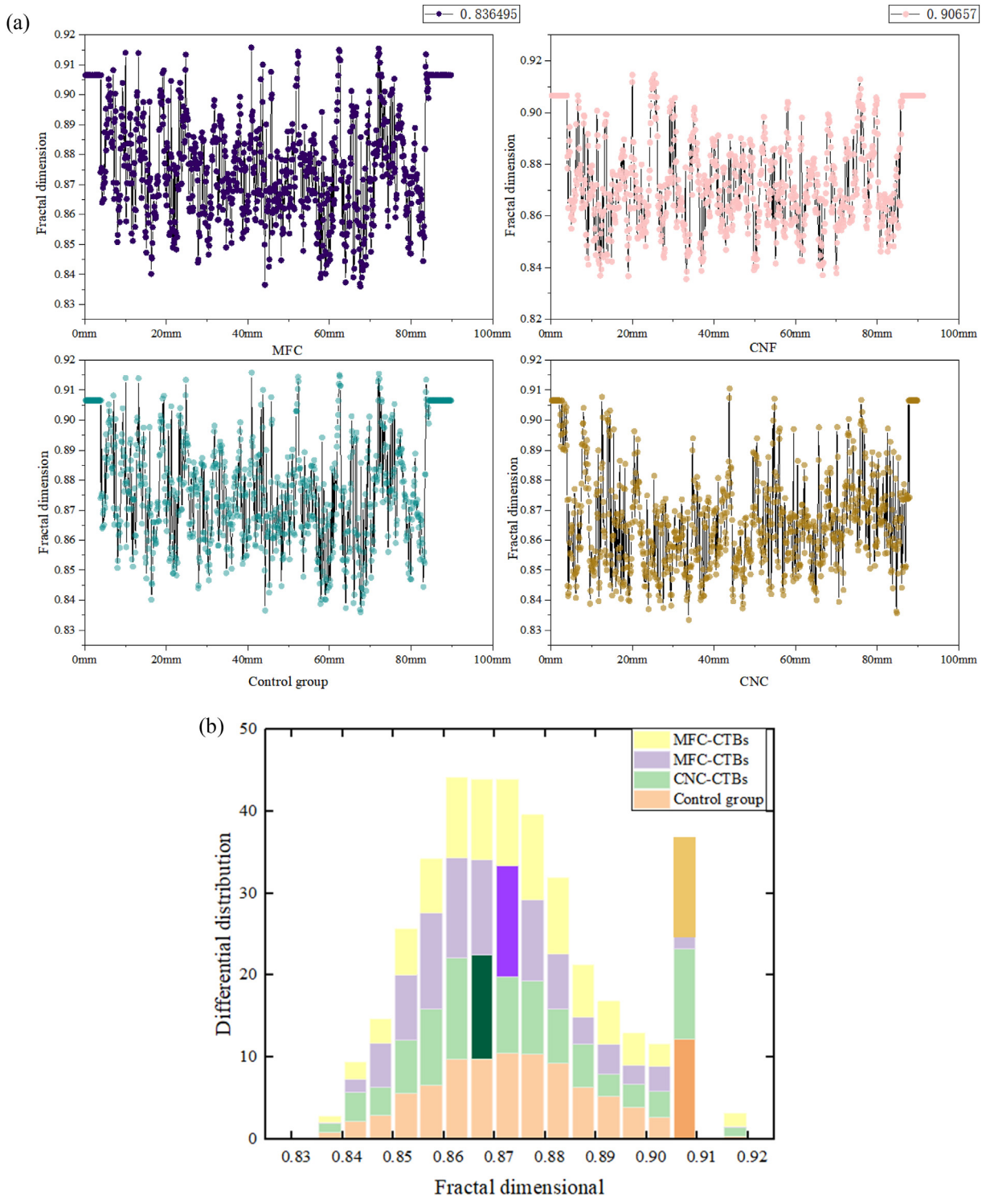

Fig. 13 – Fractal dimensional: (a) Fractal dimensional maps of different NRCTB; (b) Fractal dimension quantitative statistics chart.

with a deterioration of nearly 86%. The overall porosity of the blank control group was 21.65% porosity concentration of 10%–50%.

4.2.3. *Fractal dimensional analysis*

The fractal measurement is a degree of self-similarity and quantitative nature of the object of study, and an effective metric for measuring and comparing surface roughness. The geometric fractal can define the irregularity/complexity of material harm processes at a deeper/broader scale, and it has been shown that the geometric fractal is an efficient technique for describing pore structure [76]. Thus, this study will employ the box including dimension way to obtain NRCTB's pore fractal dimension. Here are the specific steps.

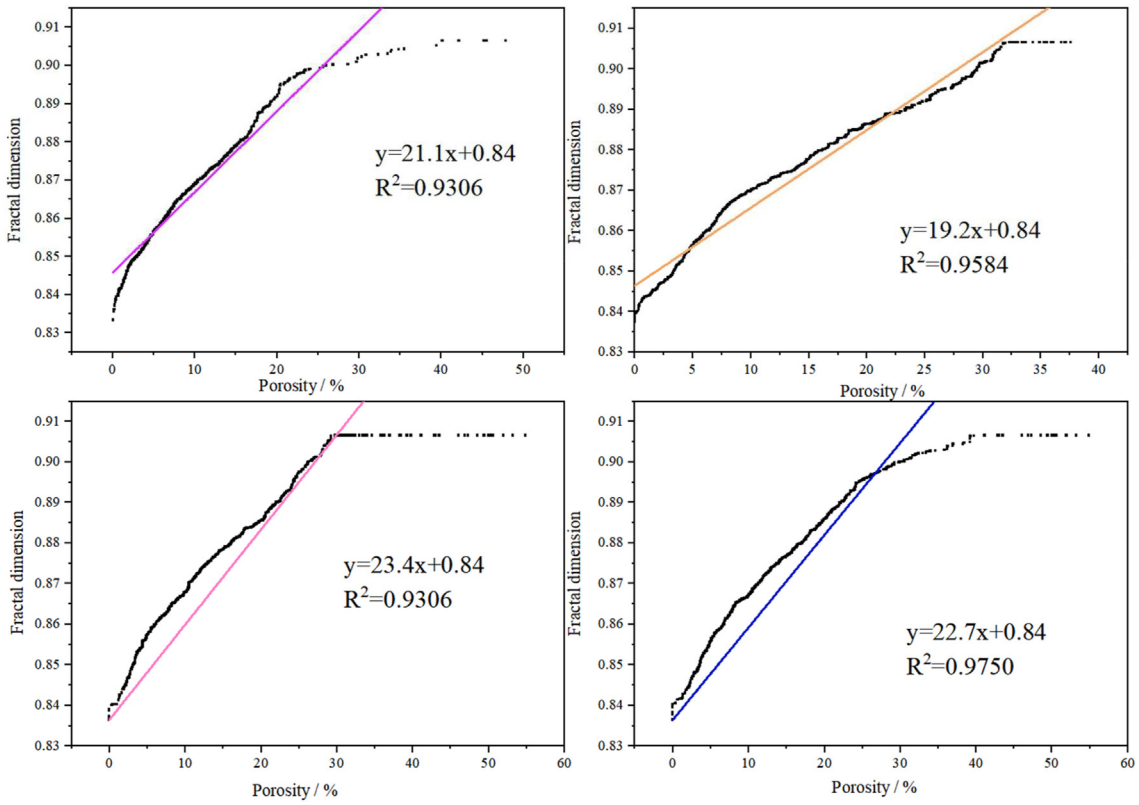

Fig. 14 – Relationship between fractal dimension and porosity.

1. Image segmentation: Choose an initial scale and divide the image into square boxes of equal size. The choice of initial scale directly affects the calculation of the fractal dimension and may need to be adjusted based on the specific characteristics of the image.
2. Object counting: For each box at each scale, count the number of objects contained within it. Objects can be features like holes, fractal structures, particles, etc.
3. Scale-object count relationship: Treat the scale as the independent variable epsilon (ε) and the number of objects within each box as the dependent variable $N(\varepsilon)$, establish a relationship between scale and object counts. By fitting a curve to the scale-object count data, a function that describes this relationship can be obtained.
4. Calculation of fractal dimension: Fractal dimension D means self-similarity and intricacy of image. By calculating the slope of the scale-object count curve, the fractal dimension can be determined. A larger slope indicates a more pronounced fractal feature and higher self-similarity.

Counting box dimension is defined as dividing the CT image into a grid with a square of side length ε. Due to the presence of NRCTB matrix in the original CT graphics, some small boxes do not cover the pores and some small boxes cover part of the pores, calculate the number of small boxes covering the pores, then reduce the box size, when the box size $\varepsilon \to 0$, the box counting dimension D_b is obtained, and the calculation formula (2):

$$D_b = \lim_{\varepsilon \to 0} \frac{\ln N(\varepsilon)}{\ln \varepsilon} \quad (2)$$

where, $N(\varepsilon)$ is the sum of small box covering pore pattern (counted as long as the grid contains pore structures,

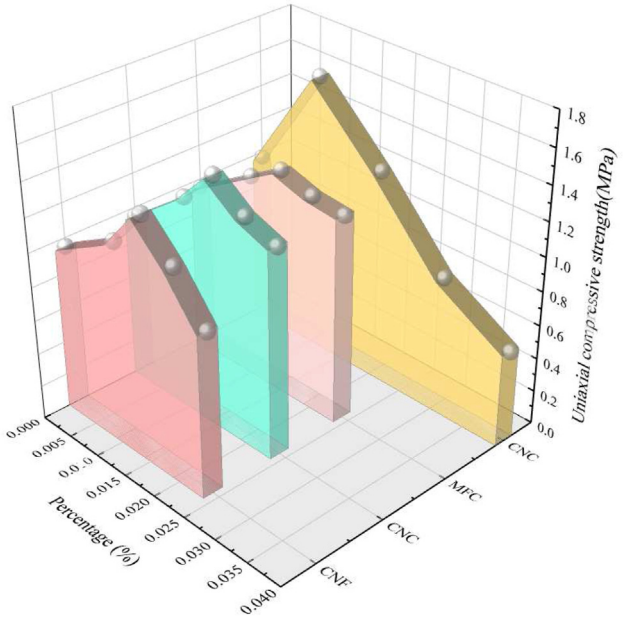

Fig. 15 – Strength of different types and concentrations of NRCTB specimens.

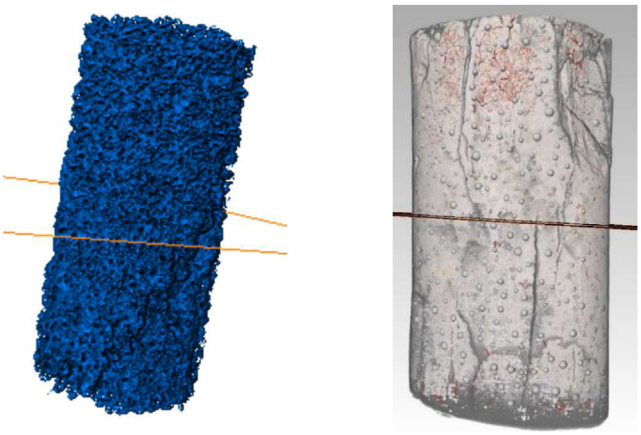

Fig. 16 – NCM 3D models: (a) CNF/CNC honeycomb network; and (b) NCM MFC ball/stick structure models.

regardless of the proportion of the grid area occupied by the pore structures); ε is the small box side length.

Under certain conditions, the higher the dimensional fractal, the more complicated pore, the value of dimensional fractal gained by box counting dimension method is exposed in Fig. 13. In general, NRCTB's fractal dimension of fluctuates up and down with large fluctuations. CNF-CTBs have a maximum value of NRCTB fractal dimension of 0.91579 at 41.0 mm height position and a minimum value of 0.835398 at 44.3 mm height position. In general, the fractal dimension of NRCTB fluctuates up and down with relatively small fluctuations; CNC-CTBs are concentrated in the fractal dimension of 0.8653. MFC-CTBs fluctuate up and down in the fractal dimension of 0.8779. Porosity and dimensional fractal are linked, and it is important to form the link between dimensional fractal and porosity to study the performance indexes of NRCTB and analyze the pore structure's characteristics, Fig. 14 shows the link between dimensional fractal and porosity. Porosity is well fitted to each other.

4.3. *Compressive strength test*

The impact of diverse NCM types on NRCTB's strength behavior was analyzed by matching the UCS of specimens with the one of NRCTB specimens. As shown in Fig. 15, the overall trend of specimens' UCS was all decreasing and then increasing, with slight differences in the changes of different types of nanocellulose curves, with slow growth phase of CNF and accelerated growth phase of MFC, while the changes of different magnitude concentrations made the trend of strength changes more obvious. The peak strength of damaged surface fracture specimens with high concentration of NRCTB with are less than NCM content of 0.009% CTBs, CNF, CNC content of 0.009% NRCTB is less than CNC-CTBs. One can interpret that the influence of strength development of NRCTB enhanced by diverse types and content of NCM will be different.

4.4. *Modeling of dual nanocellulose-pore networks for different types of NRCTB*

Clarifying the characteristic distribution of NRCTB is the base for revealing the specimen's strength mechanism. In this study, 3D level distribution characteristics of the nanocellulose of the specimen are quantitatively characterized, and considering the complicated calculation of specimen's 3D structure, a double nanocellulose-pore network model is used instead of the large-size model to study the results, which can reflect the microscopic enhancement mechanism inside the specimen in space realistically and intuitively [77]. As seen in Fig. 16, the gray part is CTBs as the matrix, and the red part is nanocellulose. This model can characterize the nanocellulose-pore structure of specimen more accurately, but due to the specimen's complex internal structure, the overall structure will be partially different from the actual one. The dual nanocellulose-pore network model can offer some reference for the microscopic enhancement mechanism inside the specimen.

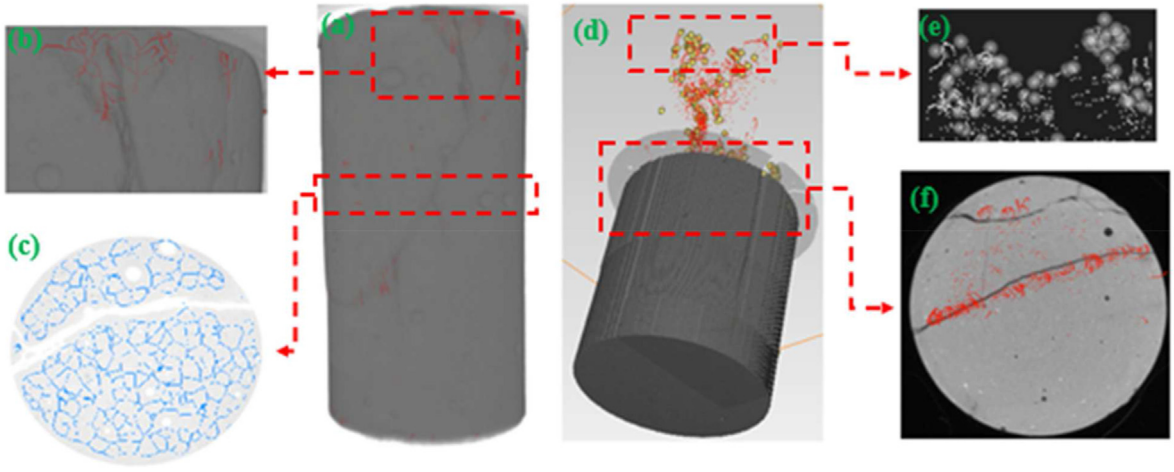

Fig. 17 – Schematic diagram of model building process: (a) CNC specimen 3D modeling; (b) CNC internal structure; (c) CNC scan image; (d) MFC specimen 3D modeling; (e) MFC internal structure; (f) MFC scan image.

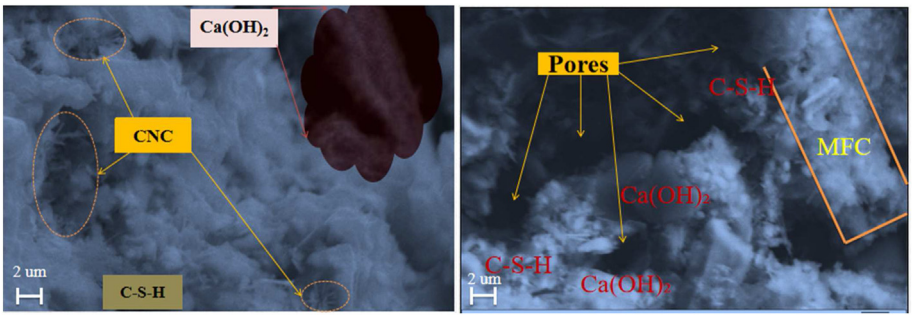

Fig. 18 – SEM images of tailing-stabilized recycled aggregates from NCM-CTBs: (a) CNC; and (b) MFC.

The CNF, CNC structure model simplified the space of NRCTB but retained the spatial distribution characteristics of NRCTB. The honeycomb network structure model is to select any point in the extracted nanocellulose mesh and extend it as the center of the sphere in all directions until it touches the nearest nanocellulose, forming a collection of all nanocellulose as the mesh structure nanocellulose. Mesh-like nanofibrils of each slice overlap with mesh-like nanofibrils of its neighboring slices to form a honeycomb mesh-like nanofibril structure model. The results of NCM honeycomb mesh model (Fig. 15) can be seen, where the blue color represents NCM. The nanocellulose network is well embedded with the pores of CT scanned specimens, and the nanocellulose honeycomb network structure modeling results are reliable.

MFC ball-and-stick model is to select any linear MFC from the extracted nanocellulose and extend it in all directions until it touches the nearest pore, with the red line representing MFC and MFC connecting the adjacent pores. The redder the color, the higher the MFC content and the better the connectivity. As shown in Fig. 16, the number of red connecting lines of specimen slices cracks increased significantly and there were multiple stitching cracks with MFC. As shown in Fig. 17, the existence of MFC amplified the sum of connected pores and enhanced porosity of MFC-CTBs.

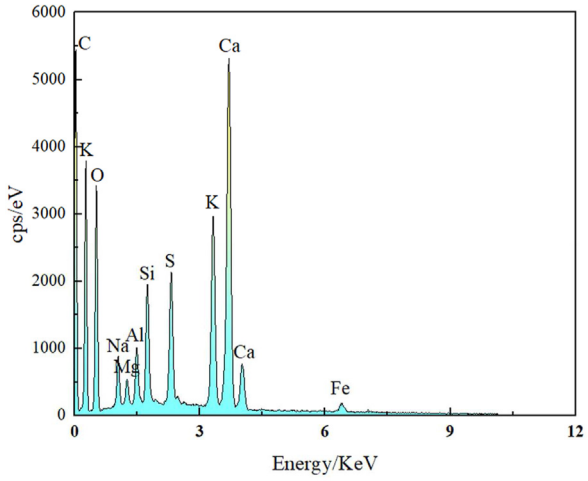

Fig. 19 – The element percentage diagram of NRCTB specimen.

4.5. *Micro analysis of NRCTB*

NCM-CTBs hydration products include calcium hydroxide, CSH gel, and hydrated calcium sulfate aluminate/calcium aluminate/calcium ferrate. CNC-CTBs hydration product CSH gel extends outward from clinker particles and gradually forms a continuous mesh structure, interspersing with other crystals to enhance adhesion and generate strength. MFC-CTBs hydration product CSH gel is gradually embedded in the fibers as the hydration product grows on the surface of the fibers, and the MFC presents a hollow structure in the matrix of the tailing sand filler, which also forms large pore size pores. The formation of CTBs' pores is influenced by the distribution of MFC, so pore structure is so connected to the content and decomposition of nanocellulose. Small size NCM can vividly increase the cementitious composites' strength development.

Its composition was analyzed by energy spectrum. Results (as shown in Fig. 19) display that hydration products are made up of C, K, O, Si, S, K, Ca, and Al. NRCTB is mainly composed of three types of products having an-hydrate cement clinker, NCM and hydration product. Fig. 18 also shows that the content of C element in NRCTB is the highest, and its components are NCM. The content of Ca element in NRCTB is the second uppermost, and its component is numerous hydration materials. Hydrated silicates typically exhibit more irregular particle shapes, whereas calcium hydroxide particles tend to be more uniform and regular. Moreover, the bulk of hydrated silicate elements is usually larger than the one of hydrated silicates in which the main elements are silicon (Si), oxygen (O), calcium (Ca) and hydrogen (H), while calcium hydroxide contains mainly calcium and oxygen elements. Nanocellulose has a large number of hydroxyl functional groups, which can interact with water molecules and adsorb on the nanocellulose surface. This surface adsorption mechanism can reduce the activity of water molecules and reduce the formation of hydrated silicates.

5. Conclusions

Based on the extensive lab tests conducted, the ensuing robust assumptions can be made regarding micro-mechanical and damage properties of NRCTBs under uniaxial compression loads and the effects of different types of nanomaterials.

1. Morphological characteristics: CNF/Enhancement CTBs exhibit isolated large cylindrical-shaped pores and uniformly distributed small pores, while MFC-CTBs mainly consist of randomly distributed slit-type pores. The control group's CTBs displayed wider and more numerous cracks, forming a crack network. The addition of nanomaterials inhibited crack formation.
2. Morphology of nanomaterials: CNF/CNC manifested a distinct complex honeycomb structure, while MFC primarily attached to the particle surface and existed between the pores.
3. Pore volumes and porosity: The pore volumes of all specimens ranged between 0.01 and 0.02 mm^3. The overall porosity of the control group was 21.65%, whereas CNC-CTBs exhibited lower porosity at 5.64%, concentrated below 10%. CNF-CTBs had an overall porosity of 11.8%, while MFC-CTBs had a higher porosity of 19.56%.
4. Fractal analysis: The porosity of NRCTB specimens disclosed a robust linear link with dimensional fractal, with a determination coefficient (R^2) of >0.9306.
5. Strength enhancement mechanisms: The dual nanocellulose-pore network model elucidated the mechanisms behind the strength enhancement in the specimens. For CNF and CNC, the strong specimen strength mechanism is based on the honeycomb network structure model, whereas MFC's enhanced strength mechanism is attributed to the ball-and-stick model.
6. Hydration products: In CNC-CTBs, the hydration product CSH gel gradually formed a continuous mesh structure, enhancing adhesion strength. In MFC-CTBs, the hydration product continuously grew on the fiber surface, gradually encapsulating the fibers. However, MFC presented a hollow structure in CTBs, resulting in the formation of large-pore size pores. Adding nanomaterials subsidized a rise in UCS values of cementitious composites.

These findings provide valuable insights into the micromechanical behavior and performance of NRCTB specimens with different nanomaterials, paving the way for further advancements in this field.

Declaration of competing interest

The authors declare that they have no conflict of interest.

Acknowledgements

The writers wish to honorably acknowledge China's National Key R&D Program (2022YFC2905004) for the generous financial support granted.

REFERENCES

[1] Cao S, Xue GL, Yilmaz E, Yin ZY. Assessment of rheological and sedimentation characteristics of cemented tailings backfill slurry. Int J Min Reclamat Environ 2021;35(5):319–35.
[2] Yang P, Suo Y, Liu L, Qu H, Xie G, Zhang C, et al. Study on the curing mechanism of cemented backfill materials prepared from sodium sulfate modified coal gasification slag. J Build Eng 2022;62:105318.
[3] Yilmaz E, Belem T, Benzaaoua M. Study of physico-chemical and mechanical characteristics of consolidated and unconsolidated cemented paste backfills. Gospodarka Surowcami Mineralnymi-Mineral Resources Management 2013;29(1):81–100.
[4] Al-Moselly Z, Fall M, Haruna S. Further insight into the strength development of cemented paste backfill materials containing polycarboxylate ether-based superplasticizer. J Build Eng 2022;47:103859.
[5] Zhao Y, Taheri A, Karakus M, Chen Z, Deng A. Effects of water content, water type and temperature on the rheological behaviour of slag-cement and fly ash-cement paste backfill. Int J Min Sci Technol 2020;30:271–8.
[6] Zhao Z, Cao S, Yilmaz E. Effect of layer thickness on flexural property and microstructure of 3D printed rhomboid polymer reinforced cemented tailings composites. Int J Miner Metall Mater 2023;30(2):236–49.
[7] Koohestani B, Mokhtari P, Yilmaz E, Mahdipour F, Darban AK. Geopolymerization mechanism of binder-free mine tailings by sodium silicate. Construct Build Mater 2021;268:121217.
[8] Rissman J, Bataille C, Masanet E, Aden N, Morrow WR, Zhou N, et al. Technologies and policies to decarbonize global industry: review and assessment of mitigation drivers through 2070. Appl Energy 2020;266:114848.
[9] Griffiths S, Sovacool BK, Kim J, Bazilian M, Uratani JM. Industrial decarbonization via hydrogen: a critical and systematic review of developments, socio-technical systems and policy options. Energy Res Social Sci 2021;80:102208.
[10] Li S, Yu Z, Hu B, Yu H, Wang X. Effect of flocculants residue on rheological properties of ultra-fine argillaceous backfilling slurry. Materials 2022;15(18):6485.
[11] Kasap T, Yilmaz E, Sari M. Effects of mineral additives and age on microstructure evolution and durability properties of sand-reinforced cementitious mine backfills. Construct Build Mater 2022;352:129079.
[12] Huang Z, Yilmaz E, Cao S. Analysis of strength and microstructural characteristics of mine backfills containing fly ash and desulfurized gypsum. Minerals 2021;11(4):409.
[13] Kamasamudram KS, Ashraf W, Landis E. Cellulose nanofibrils with and without nanosilica for the performance enhancement of Portland cement systems. Construct Build Mater 2021;285:121547.
[14] Yilmaz E, Belem T, Benzaazoua M, Kesimal A, Ercikdi B, Cihangir F. Use of high-density paste backfill for safe disposal of copper/zinc mine tailings. Gospodarka Surowcami Mineralnymi-Mineral Resources Management 2011;27(3):81–94.
[15] Zhang X, Xu M, Liu L, Huan C, Zhao Y, Qi CC, et al. Experimental study on thermal and mechanical properties of cemented paste backfill with phase change material. J Mater Res Technol 2020;9(2):2164–75.
[16] Ferreira SR, Ukrainczyk N, Silva KDC, Silva LE, Koenders E. Effect of microcrystalline cellulose on geopolymer and Portland cement pastes mechanical performance. Construct Build Mater 2021;288:123053.
[17] Benzaazoua M, Belem T, Yilmaz E. Novel lab tool for paste backfill. Can Min J 2006;127(3):31–2.
[18] Dufresne A. Nanocellulose: a new ageless bionanomaterial. Mater Today 2013;16:220–7.
[19] Thomas B, Raj MC, Athira KB, Rubiyah MH, Joy J, Moores A, et al. Nanocellulose, a versatile green platform: from biosources to materials and their applications. Chem Rev 2018;118(24):11575–625.

[20] De France KJ, Hoare T, Cranston ED. Review of hydrogels and aerogels containing nanocellulose. Chem Mater 2017;29:4609–31.
[21] Metaxa ZS, Tolkou AK, Efstathiou S, Rahdar A, Favvas EP, Mitropoulos AC, et al. Nanomaterials in cementitious composites: an update. Molecules 2021;26(5):1430.
[22] Konsta-Gdoutos MS, Batis G, Danoglidis PA, Zacharopoulou AK, Zacharopoulou EK, Falara MG, et al. Effect of CNT and CNF loading and count on the corrosion resistance, conductivity and mechanical properties of Nano-modified OPC mortars. Construct Build Mater 2017;147:48–57.
[23] Deepa B, Abraham E, Cordeiro N, Mozetic M, Mathew AP, Oksman K, et al. Utilization of various lignocellulosic biomass for the production of nanocellulose: a comparative study. Cellulose 2015;22:1075–90.
[24] Toivonen MS, Kaskela A, Rojas OJ, Kauppinen EI. Ambient-dried cellulose nanofibril aerogel membranes with high tensile strength and their use for aerosol collection and templates for transparent, flexible devices. Adv Funct Mater 2015;25:6618–26.
[25] Varisha MM Zaheer, SD Hasan. Mechanical and durability performance of carbon nanotubes (CNTs) and nanosilica (NS) admixed cement mortar. Mater Today Proc 2021;42(2):1422–31.
[26] Haque MI, Ashraf W, Khan R, Shah S. A comparative investigation on the effects of nanocellulose from bacteria and plant-based sources for cementitious composites. Cement Concr Compos 2022;125:104316.
[27] Wang A, Cao S, Yilmaz E. Influence of types and contents of nano cellulose materials as reinforcement on stability performance of cementitious tailings backfill. Construct Build Mater 2022;344:128179.
[28] Stephens C, Brown L, Sanchez F. Quantification of the re-agglomeration of carbon nanofiber aqueous dispersion in cement pastes and effect on the early age flexural response. Carbon 2016;107:482–500.
[29] Fan QC, Meng X, Li Z, Ma G, Wang Z, Zhang K, et al. Experiment and molecular dynamics simulation of functionalized cellulose nanocrystals as reinforcement in cement composites. Construct Build Mater 2022;341:127879.
[30] Siqueira IS, Dweck J, Filho RDT. Effect of microcrystalline and micro-fibrillated cellulose on the evolution of hydration of cement pastes by thermogravimetry. J Therm Anal Calorim 2020;142:1413–28.
[31] Cui J, Yuan X, Wu S, Zhang R, Jin S, Li Y. Rock types and reservoir characteristics of shahejie formation marl in Shulu Sag, Jizhong depression, Bohai Bay basin. J Earth Sci 2021;32:986–97.
[32] Chalmers GR, Bustin RM, Power IM. Characterization of gas shale pore systems by porosimetry, pycnometry, surface area, and field emission scanning electron microscopy/transmission electron microscopy image analyses: examples from the Barnett. Woodford, Haynesville, Marcellus, and Doig units, Archives 2012;96(6):1099–119.
[33] Huang ZQ, Cao S, Yilmaz E. Microstructure and mechanical behavior of cemented gold/tungsten mine tailings-crushed rock backfill: effects of rock gradation and content. J Environ Manag 2023;339:117897.
[34] Deng H, Hu X, Li HA, Luo B, Wang W. Improved pore-structure characterization in shale formations with FESEM technique. J Nat Gas Sci Eng 2016;35:309–19.
[35] Ma L, Slater T, Dowey PJ, Yue S, Rutter EH, Taylor KG, et al. Hierarchical integration of porosity in shales. Sci Rep 2018;8:11683.
[36] Mirtalebi E, Shirazi MMA, Kargari A, Tabatabaei M, Ramakrishna S. Assessment of atomic force and scanning electron microscopes for characterization of commercial and electrospun nylon membranes for coke removal from wastewater. Desalination Water Treat 2014;52:6611–9.
[37] Yao YB, Liu DM, Cai YD, Li JQ. Advanced characterization of pores and fractures in coals by nuclear magnetic resonance and X-ray computed tomography. Sci China Earth Sci 2010;53:854–62.
[38] Cheng Z, Ning Z, Zhao H, Wang Q, Zeng Y, Wu X, et al. A comprehensive characterization of North China tight sandstone using micro-CT, SEM imaging, and mercury intrusion. Arabian J Geosci 2019;12:407.
[39] Ghamgosar M, Erarslan N, Williams DJ. Experimental investigation of fracture process zone in rocks damaged under cyclic loadings. Exp Mech 2017;57:97–113.
[40] Kumari WGP, Ranjith PG, Perera MSA, Li X, Li LH, Chen BK, et al. Hydraulic fracturing under high temperature and pressure conditions with micro CT applications: geothermal energy from hot dry rocks. Fuel 2018;230:138–54.
[41] Wang SY, Lin CL, Li S, Chen M, Lu Y. Effect of CNFs on the mechanical properties and microstructure of early strength seawater sea-sand engineered cementitious composites. Construct Build Mater 2021;307:124961.
[42] Hammat S, Menadi B, Kenal S, Thomas C, Kirgiz MS, de Sousa Galdino AG. The effect of content and fineness of natural pozzolana on the rheological, mechanical, and durability properties of self-compacting mortar. J Build Eng 2021;44:103276.
[43] Li JJ, Yilmaz E, Cao S. Influence of industrial solid waste as filling material on mechanical and microstructural characteristics of cementitious backfills. Construct Build Mater 2021;299:124288.
[44] Hu JH, Ren QF, Ma SW, Jiang Q, Jiang YJ, Shang JL, et al. Macroscopic and microscopic trans-scale characteristics of pore structure of mine grouting materials. Trans Nonferrous Metals Soc China 2019;29:1067–81.
[45] Wang AA, Cao S, Yilmaz E. Effect of height to diameter ratio on dynamic characteristics of cemented tailings backfills with fiber reinforcement through impact loading. Construct Build Mater 2022;322:126448.
[46] Yu X, Kemeny J, Tan Y, Song W, Huang K. Mechanical properties and fracturing of rock-backfill composite specimens under triaxial compression. Construct Build Mater 2021;304:124577.
[47] Zhang H, Cao S, Yilmaz E. Influence of 3D-printed polymer structures on dynamic splitting and crack propagation behavior of cementitious tailings backfill. Construct Build Mater 2022;343:128137.
[48] Sun W, Hou K, Yang Z, Wen Y. X-ray CT three-dimensional reconstruction and discrete element analysis of the cement paste backfill pore structure under uniaxial compression. Construct Build Mater 2017;138:69–78.
[49] Huang Z, Cao S, Yilmaz E. Investigation on the flexural strength, failure pattern and microstructural characteristics of combined fibers reinforced cemented tailings backfill. Construct Build Mater 2021;300:124005.
[50] Li B, Zhang G, Wang G, Qiao J. Damage evolution of frozen-thawed granite based on high-resolution computed tomographic scanning. Front Earth Sci 2022;10:912356.
[51] Martínez-Martínez J, Fusi N, Galiana-Merino JJ, Benavente D, Crosta GB. Ultrasonic and X-ray computed tomography characterization of progressive fracture damage in low-porous carbonate rocks. Eng Geol 2016;200:47–57.
[52] Alp I, Deveci H, Sungun YH, Yilmaz AO, Kesimal A, Yilmaz E. Pozzolanic characteristics of a natural raw material for use in blended cements. Iran J Sci Technol Trans B-Eng 2009;33(4):291–300.
[53] Zhou JZ, Yu TQ, Xu XH. Fractal analysis of damage evolution of rock. Int J Damage Mech 2000;9(4):378–86.

[54] Nazarchuk Z, Andreykiv O, Skalskyi V, Rudavskyi D. Acoustic emission method in the delayed fracture mechanics of structural materials. Procedia Struct Integr 2019;16:169–75.
[55] Chen M, Sun L, Hong Z, Wang H, Xia Y, Liu S, et al. Anthracene single-crystal scintillators for computer tomography scanning. ACS Appl Mater Interfaces 2022;14(36):41275–82.
[56] Chen SM, Yilmaz E, Wang W, Wang YM. Curing stress effect on stability, microstructure, matric suction and electrical conductivity of cementitious tailings backfills. Construct Build Mater 2022;360:129601.
[57] Xue GL, Yilmaz E, Feng GR, Cao S, Sun LJ. Reinforcement effect of polypropylene fiber on dynamic properties of cemented tailings backfill under SHPB impact loading. Construct Build Mater 2021;279:122417.
[58] Bharath G, Shukla M, Chandra S, Shaw A. Laboratory and field evaluation of cement grouted bituminous mixes. Road Mater Pavement Des 2020;21(6):1694–712.
[59] Tian W, Dang F, Liang X. CT image analysis of meso fracture process of concrete. Engineering Journal of Wuhan University 2008;41:69–72.
[60] Gallucci E, Scrivener K, Groso A, Stampanoni M, Margaritondo G. 3D experimental investigation of the microstructure of cement pastes using synchrotron X-ray microtomography (μCT). Cement Concr Res 2007;37(3):360–8.
[61] Ren W, Yang Z, Sharma R, Zhang C, Withers PJ. Two-dimensional X-ray CT image based meso-scale fracture modelling of concrete. Eng Fract Mech 2015;133:24–39.
[62] Zhang P, Qin HG, Wan K, Pang C, Sun W, Zhou W. Application of X-CT technology in the microstructure analysis of cement-based materials. Appl Mech Mater 2012;174(9):2061–4.
[63] Sainz-Aja J, Carrascal I, Polanco JA, Thomas C. Fatigue failure micromechanisms in recycled aggregate mortar by μCT analysis. J Build Eng 2020;28:101027.
[64] Yi C, Zhu HG, Liu LZ. Damage analysis for quasi-birttle materials of CT image under uniaxial compression. Adv Mater Res 2010;373(9):168–70.
[65] Zhao L, Li C, Dang F, Chen D. Architecture concrete mesostructure analysis based on CT image fracture process. Adv Mater Res 2013;368–373:2638–41.
[66] Jianhua H, Quan J, Qifan R. Cross scale correlation characteristics of pore structure and meso parameters of filling body. Chin J Nonferrous Metals 2018;28:2154–63.
[67] Hu J, Ding X, Ren Q, Luo Z, Jiang Q. Effect of incorporating waste limestone powder into solid waste cemented paste backfill material. Appl Sci 2019;9(10):2076.
[68] Yue D, Xiao Y, Qian G. Research on effect of pore characteristics on performance of aerated backfilling concrete based on imaging method. Mater Rev 2018;32(9):3128–34.
[69] Gang W, Xiang Q, Cheng J. Simulations of temperature effects on seepage and deformation of coal microstructure in 3D CT reconstructions. Rock Soil Mech 2020;41(5).
[70] Zhang H, Cao S, Yilmaz E. Carbon nanotube reinforced cementitious tailings composites: links to mechanical and microstructural characteristics. Construct Build Mater 2023;365:130123.
[71] Li JJ, Cao S, Yilmaz E, Liu YP. Compressive fatigue behavior and failure evolution of additive fiber-reinforced cemented tailings composites. Int J Miner Metall Mater 2022;29(2):345–55.
[72] Arendse E, Fawole OA, Magwaza LS, Opara UL. Non-destructive characterization and volume estimation of pomegranate fruit external and internal morphological fractions using X-ray computed tomography. J Food Eng 2016;186:42–9.
[73] Cnudde V, Masschaele B, Dierick M, Vlassenbroeck J, Van Hoorebeke L, Jacobs P. Recent progress in X-ray CT as a geosciences tool. Appl Geochem 2006;21(5):826–32.
[74] Okabe H, Blunt MJ. Prediction of permeability for porous media reconstructed using multiple-point statistics. Phys Rev 2004;70(6):066135.
[75] Aadland RC, Jakobsen TD, Heggset EB, Long-Sanouiller H, Simon S, Paso KG, et al. High-temperature core flood investigation of nanocellulose as a green additive for enhanced oil recovery. Nanomaterials 2019;9(5):665.
[76] Xia Y, Cai J, Wei W, Hu X, Wang X, Ge X. A new method for calculating fractal dimensions of porous media based on pore size distribution. Fractals 2018;26(1).
[77] Fang K, Fall M, Cui L. Thermo-chemo-mechanical cohesive zone model for cemented paste backfill-rock interface. Eng Fract Mech 2021;244:107546.